Double-Weyl Phonons in Transition-Metal Monosilicides

Tiantian Zhang,[1,4] Zhida Song,[1,4] A. Alexandradinata,[2] Hongming Weng,[1,3] Chen Fang,[1,*] Ling Lu,[1,†] and Zhong Fang[1,3]
[1]Institute of Physics, Chinese Academy of Sciences/Beijing National Laboratory for Condensed Matter Physics, Beijing 100190, China
[2]Department of Physics, Yale University, New Haven, Connecticut 06520, USA
[3]Collaborative Innovation Center of Quantum Matter, Beijing 100084, China
[4]University of Chinese Academy of Sciences, Beijing 100049, China

(Received 25 June 2017; published 5 January 2018)

We employed *ab initio* calculations to identify a class of crystalline materials of MSi (M = Fe, Co, Mn, Re, Ru) having double-Weyl points in both their acoustic and optical phonon spectra. They exhibit novel topological points termed "spin-1 Weyl point" at the Brillouin zone center and "charge-2 Dirac point" at the zone corner. The corresponding gapless surface phonon dispersions are two helicoidal sheets whose isofrequency contours form a single noncontractible loop in the surface Brillouin zone. In addition, the global structure of the surface bands can be analytically expressed as double-periodic Weierstrass elliptic functions.

DOI: 10.1103/PhysRevLett.120.016401

Topological states of electrons [1–4] and photons [5,6] have attracted significant interest recently. Topological mechanical states [7–21], also being actively explored, have only been limited to low-energy classical sound waves at kHz frequencies in macroscopic artificial lattices. However, the important processes like heat conduction and electron-phonon coupling are all determined by THz phonons of atomic lattice vibrations, whose force constants have to be evaluated quantum mechanically. In this Letter, we explore crystalline materials in the noncentrosymmetric space group $P2_13$ (No.198), whose threefold representation at Brillouin zone (BZ) center and fourfold representations at BZ edge are point degeneracies of Chern number 2. A class of transition-metal monosilicides are consequently found to host such double Weyl points throughout their phonon spectrum of terahertz frequencies. The double-Weyl surface states are explicitly calculated and can be analytically described by the Weierstrass elliptic function. Our prediction of topological bulk and surface phonons can be experimentally verified by many techniques [22] such as neutron scattering [23] for bulk phonons and electron energy loss spectroscopy [24] for surface phonons. This work paves the way for topological phononics [25–28] at the atomic scale.

Double Weyl points.— The two-band Hamiltonian near a Weyl point [29–36] [Fig. 1(a)], $H_2(\mathbf{k}) \propto \mathbf{k}\cdot\mathbf{S} = (\hbar/2)\mathbf{k}\cdot\boldsymbol{\sigma}$, is the simplest possible Lorentz invariant theory for three-dimensional (3D) massless fermions, where $\mathbf{S}$ is the rotation generator for spin-1/2 particles and σ_i's are the Pauli matrices. The two bands have spin components $S_k = \mathbf{S}\cdot\hat{\mathbf{k}} = +\hbar/2$ and $-\hbar/2$ and form inward or outward hedgehog configuration on each equal-energy surface. The Chern number of $+1$ or -1 is the topological invariant that distinguishes between these two cases. For spin-1 bosons like phonon, photon and magnons, the natural extension of a Weyl Hamiltonian is the three-band Hamiltonian $H_3(\mathbf{k}) \propto \mathbf{k}\cdot\mathbf{L}$ [Fig. 1(c)], where L_i are the spin-1 matrix representations of the rotation generators. The Chern numbers of the resultant three bands, corresponding to $L_k = \mathbf{L}\cdot\hat{\mathbf{k}} = \hbar, 0, -\hbar$ are $+2$, 0 and -2, doubling those of the spin-1/2 Weyl point. We hence refer to such a band crossing point as the "spin-1 Weyl point" [37] in this paper. Another possibility of band crossing having Chern number of 2 is the direct sum of two identical spin-1/2 Weyl points, referred to as "charge-2 Dirac point" in this paper [Fig. 1(d)], whose four-band Hamiltonian is $H_4(k) \sim \left(\begin{smallmatrix}\mathbf{k}\cdot\boldsymbol{\sigma} & 0\\ 0 & \mathbf{k}\cdot\boldsymbol{\sigma}\end{smallmatrix}\right)$ [38], in contrast to a regular 3D Dirac point consists of two Weyl points of opposite Chern numbers [39] and quadratic double-Weyl points between two bands [40–43] [Fig. 1(b)]. In the following, we show the presence of the spin-1 Weyl and charge-2 Dirac points in the phonon spectra of existing materials.

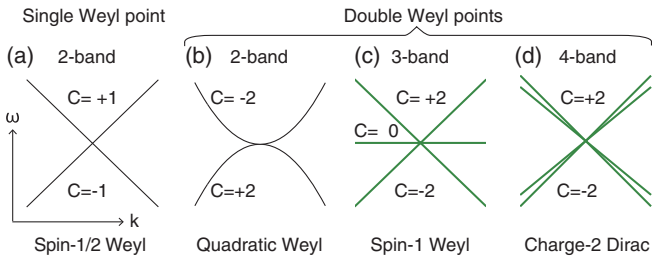

FIG. 1. Single Weyl point and two types of double-Weyl points. (a) A spin-1/2 Weyl point of Chern number of ± 1. (b) The 2-band quadratic Weyl point with Chern numbers of ± 2. (c) The 3-band spin-1 Weyl point with Chern numbers of 0, ± 2. (d) The 4-band charge-2 Dirac point with Chern numbers ± 2. Here we refer to quadratic Weyl point, spin-1 Weyl point and charge-2 Dirac points as double Weyl points. We focus on the 3-band and 4-band double Weyl points in this paper.

Phonon calculations.— Phonons are quantized excited vibrational states of interacting atoms. Solids with more than one atom in the primitive cell have both acoustic and optical branches in their phonon band structure, which we computed for the *M*Si family (M = Fe, Co, Mn, Re, Ru) in Fig. 2. *M*Si belongs to the simple cubic crystal structure with space group $P2_13$ (No. 198). Each primitive cell contains 8 atoms, both M and Si atoms occupy Wyckoff positions (4a). The crystal structure of *M*Si [44,45] is shown in Fig. 2(a) and the corresponding BZ is shown in Fig. 2(b). In this paper, the phonon force constants are calculated based on density functional perturbation theory [46], using Vienna *ab initio* simulation package (VASP) [47]. Wilson loop method [48,49] is used to find the Chern numbers of the double-Weyl points.

Spin-1 Weyl acoustic phonons.— Shown in Fig. 2(c), the three branches of acoustic phonons form a spin-1 Weyl point. The longitudinal branch has a Chern number of 0 and the two transverse branches have Chern numbers of ± 2, reflecting the fact that phonons are spin-1 particles. We note that the individual Chern numbers can be defined only when the three acoustic dispersions are well separated from each other. This only happens when $\mathcal{PT}$ symmetry is broken, since, otherwise, Berry curvature strictly vanishes and the Chern number of any band is zero. Here $\mathcal{P}$ is parity inversion and $\mathcal{T}$ is time reversal. *M*Si is noncentrosymmetric, so $\mathcal{P}$ is broken in the lattice. We emphasize that these spin-1 Weyl dispersions is a general property for both phonons and photons at zero frequency; the difference lies in the vanishing longitudinal mode for photons [50]. We note that the topological surface states related to this zero-frequency spin-1 Weyl point may not be observed, since the two transverse Chern bands both have positive group velocity in all directions, not leaving a bulk gap when projected on any open surface.

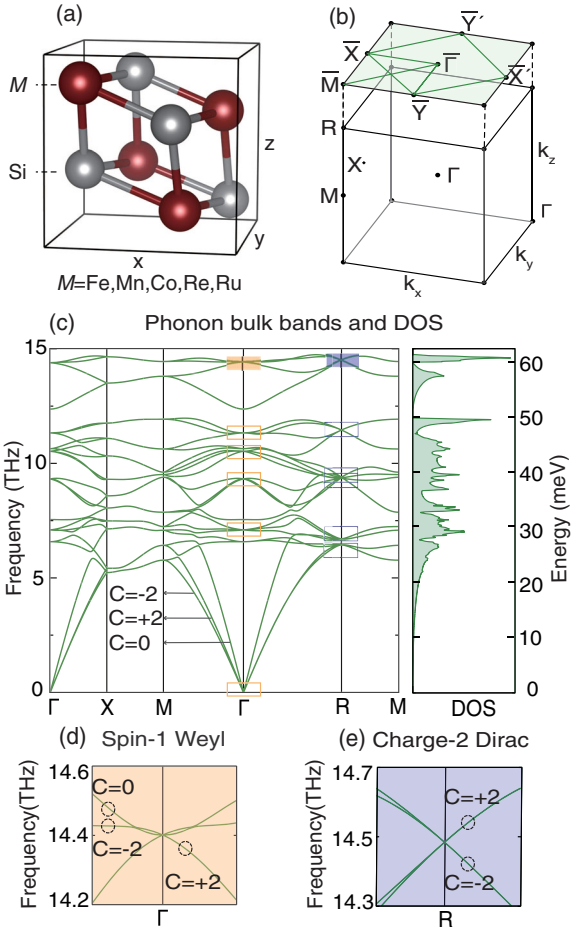

FIG. 2. *M*Si crystal structure and phonon bands. (a) Cubic unit cell contains 4 M and 4 Si atoms. (b) Bulk and (001) surface BZs. (c) Phonon dispersion of FeSi along high-symmetry directions. The acoustic bands have Chern numbers of $0, \pm 2$. The orange boxes are centered around the spin-1 Weyl points at Γ and the purple boxes are centered around the charge-2 Dirac points at R. (d) Γ point is a spin-1 Weyl point. (e) R point is a charge-2 Dirac point.

Double-Weyl optical phonons.— Both the spin-1 Weyl points at Γ and charge-2 Dirac points at R were found in the optical phonon spectrum of FeSi in Fig. 2(c). They are stabilized by the lattice symmetries and $\mathcal{T}$. The No. 198 ($P2_13$) space group has twofold screw rotations along each $\langle 100 \rangle$ axes ($\{C_{2x}|(\frac{1}{2},\frac{1}{2},0)\}$ along x axis) and threefold rotations C_3 along the $\langle 111 \rangle$ axes. We performed a $k \cdot p$ analysis at the two $\mathcal{T}$-invariant momenta of Γ and R (see Sec. IV of the Supplemental Material [51] for details).

At the Γ point, the irreducible representations for the optical branches are $\Gamma = 2A + 2E + 5T$, in which A, E, and T represent the singly, doubly, and triply degenerate multiplets, respectively. All five threefold band degeneracies are spin-1 Weyl points enforced by the little group symmetry at Γ, which is the point group $T(23)$. The polariton effect of LO-TO splitting is discussed in the Supplemental Material [51].

At the R point of the BZ corner, all bands form charge-2 Dirac points. In other words, in *M*Si materials, every phonon band connects to the fourfold degenerate double-Weyl points at R. This is due to both $\mathcal{T}$ and the nonsymmorphic nature of the No. 198 space group containing three screw axes.

As examples, we plotted the closeup dispersions of the two types of double-Weyl points of the highest phonon bands (~14.5 THz) in Figs. 2(d) and 2(e). These four bands are frequency isolated from the rest. Since a topological point carrying nonzero Chern number cannot exist alone in the BZ, the spin-1 Weyl and charge-2 Dirac points come in pairs and their Chern numbers cancel exactly.

Here we offer an intuitive perspective to understand the charge-2 Dirac point at R. The three screw axes, $C_{2x,2y,2z}$, at this point anticommute with each other and satisfy $C_{2i}^2 = -1$, just like half-integer spin rotations. From this we know that all irreducible representations have even dimensions, with the smallest representation being two dimensional and the rotations represented by $\pm i\sigma_{x,y,z}$.

But since R is also time-reversal invariant, these screw axes must commute with $\mathcal{T}$, so that all matrice representations of the three screws must be real. This is impossible for two-dimensional representations of SU(2), but can be met by four-dimensional representations. Finally, since time reversal preserves the Chern number of a Weyl point, the four-dimensional representation has charge ± 2.

Single noncontractible surface loop.— An isoenergy contour of any 2D (noninteracting) system or trivial surface state is a closed loop, which can be continuously deformed into an even number of noncontractible loops which wraps around the BZ torus. The unique feature of a Weyl crystal is its open surface arcs whose ends are pinned by the projection of Weyl points in the bulk. In contrast, the MSi surface contour is a single noncontractible loop.

The surface local density of states (LDOS) is plotted along the surface momentum lines in Fig. 3(a) and the iso-frequency surface contours are plotted in Figs. 3(b), 3(c), and 3(d) for different frequencies. For computing the surface LDOS, we first calculated the second rank tensor of force constant in Cartesian coordinates from density functional perturbation theory, from which we can get the tight-binding parameters for the bulk and surface atoms. [52]. Then we obtain the surface Green's function iteratively and take its imaginary part as the LDOS [53–55].

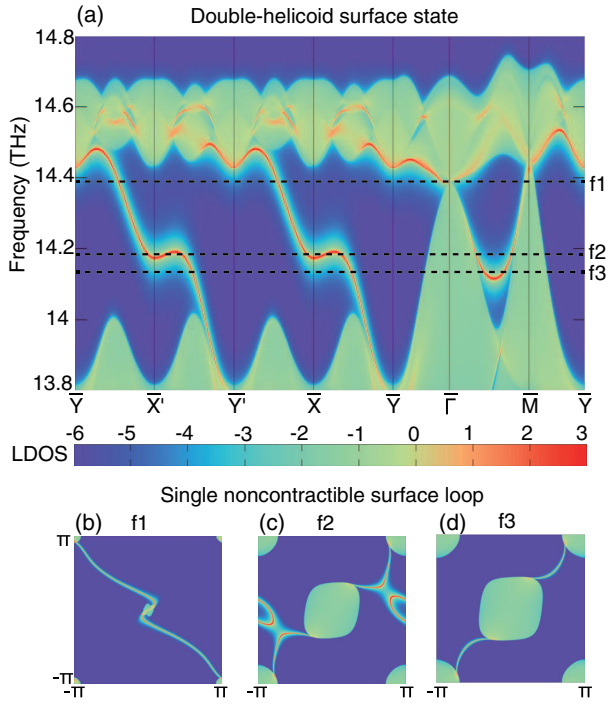

FIG. 3. Double-helicoid surface states and noncontractable surface arcs. (a) The surface LDOS for the (001) surface along high-symmetry directions. The corresponding surface arcs for different frequency are showed in (b)–(d), plotted in the log scale. There are two arcs rotates around the two double Weyl points as the frequency decreases from f1 to f3, which demonstrates the double-helical surface states.

On the (001) surface, the symmetries of the MSi lattice are broken on the surface and $\mathcal{T}$ is the only symmetry left invariant other than the in-plane translations. The (001) surface BZ is a square. The spin-1 Weyl point at Γ is projected to $\bar{\Gamma}$, and the charge-2 Dirac point at R is projected to $\bar{M}$. Note that the four BZ corners are the same $\bar{M}$ point. Since surface arcs always connect two Weyl points with opposite Chern numbers, there should be two arcs connecting the double-Weyl points at the BZ center ($\bar{\Gamma}$) and BZ corner ($\bar{M}$). Constrained by $\mathcal{T}$, the two arcs must be related by a π rotation about Γ; when viewed together, the two arcs stretch diagonally across the BZ. This forms a single noncontractible loop connected by two surface arcs where the connection points are projections of the bulk double-Weyl points. These novel noncontractible surface loops are shown at three different frequencies in Figs. 3(b), 3(c), and 3(d), where the bulk pockets are connected by the two arcs.

Double-helicoid surface states.— Isoenergy surface arcs are only the local description (in energy) of a topological surface state in the momentum space, which are gapless under arbitrary surface conditions, in the presence of the protecting symmetries. They are sheets noncompact (not bounded) and gapless along the frequency axis. Fang *et al.* [56] pointed out that the Weyl surface states are equivalent to a helicoid, one of the common noncompact Riemann sheets. Here, it is natural to expect that the surface state of a double-Weyl crystal is a double helicoid: two surface sheets wind around the double Weyl point. This is indeed confirmed by the results plotted in Fig. 3 and illustrated in Fig. 4.

Analytical description by Weierstrass elliptic function.— We show that the double-helicoid surface of MSi phonons

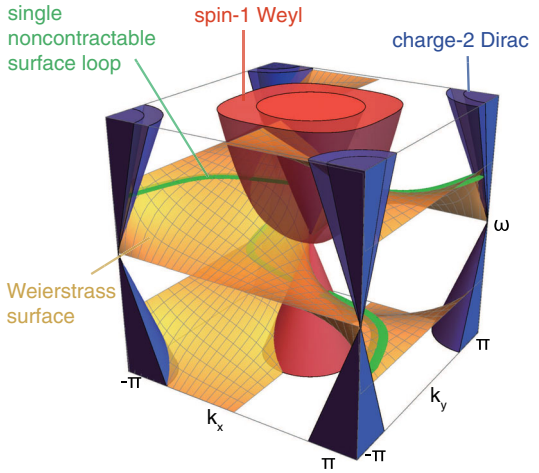

FIG. 4. The double-helicoid surface state is described by the Weierstrass elliptic function. The red spin-1 Weyl point corresponds to the double zero point and the blue charge-2 Dirac point corresponds to the double pole point. Two yellow surfaces rotate around these two double-Weyl points as double helicoids.

is topologically equivalent to the Weierstrass elliptic function, that is double-periodic and analytical in the whole BZ. In Ref. [56], Fang *et al.* showed that the surface state dispersion near the projection of topological band crossings can be mapped to the Riemann surfaces of analytic functions with surface momentum $k \equiv k_x + ik_y$ as a complex variable. Near the projection of a Weyl point having Chern number (C), the dispersion is topologically equivalent to the winding phase of an analytic function having an order-C zero ($C > 0$) or pole ($C < 0$), or symbolically $\omega(z) \sim \mathrm{Im}[\log(z^C)]$, where z is the planar momentum relative to the projection of the Weyl point.

However, this analytic functions z^C is defined in a noncompact momentum space and hence cannot provide a global description for surface dispersions in the whole surface BZ, which is a compact torus. To establish the global picture, we notice that analytic functions having two or more zero-pole pairs and are periodic in both directions are elliptic functions. Therefore, we use the Weierstrass elliptic function ($\wp$), having one second-order pole at $\mathbf{k}_+ = (\pi, \pi)$ and one second-order zero at $\mathbf{k}_- = (0, 0)$, to reveal the global structure of the double-Weyl surface states. The explicit mapping is given by

$$\omega(k_x, k_y) \sim \wp(z; 2\pi, 2\pi) = \mathrm{Im}\left\{\log\left[\frac{1}{z^2} + \sum_{n,m\neq 0}\left(\frac{1}{(z + 2m\pi + 2n\pi i)^2} - \frac{1}{(2m\pi + 2n\pi i)^2}\right)\right]\right\}, \quad (1)$$

where $z \equiv k - (1 + i)\pi$.

We plot, in Fig. 4, the Weierstrass surface state in the whole BZ with the illustrated bulk double-Weyl points at the pole and zero. The isofrequency surface loops have alternating orientations as the frequency changes. Two loops are plotted in green that match the calculation results in Figs. 3(b) and 3(c). This indicates that the surface phonons propagate towards different directions at different energies.

Conclusion.— We predicted topological phonons in both acoustic and optical branches of a family of existing crystalline materials: transition-metal monosilicides, that was previously studied as thermal-electric materials [57,58] and superconductors [59]. Experimentally, bulk phonons can be measured by neutron scattering [23] or x-ray scattering [60] and surface phonons can be probed by high resolution electron energy loss spectroscopy [24], helium scattering [61], or THz spectroscopy [62,63]. Low-temperature measurements might be helpful to minimize the anharmonic effects (see Supplemental Material [51]). Topological bulk phonons could be advantageous for phonon transport [64], around the frequencies of the Weyl nodes, due to their linear dispersions and reduced backscattering. Topological surface phonons can potentially enhance electron-phonon interactions at material interfaces, since they are guaranteed to localize at the surface [65,66]. This is beneficial, for example, to interfacial superconductivity [67].

We thank Jiawei Zhou, Yuanfeng Xu, Gregory Moore, Shiyan Li, Xuetao Zhu for useful discussion. This work was supported National key R&D Program of China under Grants No. 2016YFA0302400 (C. F, L. L.), No. 2016YFA0300600 (C. F., H. W.), and No. 2017YFA0303800 (L. L.), NSFC under Grants No. 11674370 (C. F.), No. 11421092 (T. Z., H. W., Z. F.), and No. 11721404 (L. L.), the National 973 program of China No. 2013CB921700 (Z. F.), the Yale Postdoctoral Prize Fellowship (A. A.), and the National Thousand-Young Talents Program of China (C. F., L. L.).

Note added.—Recently, we became aware of two related works reporting multiple Weyl fermions, instead of phonons, in the same material system [68,69].

*cfang@iphy.ac.cn
†linglu@iphy.ac.cn

[1] M. Z. Hasanand C. L. Kane, Colloquium: Topological insulators, Rev. Mod. Phys. **82**, 3045 (2010).
[2] X.-L. Qi and S.-C. Zhang, Topological insulators and superconductors, Rev. Mod. Phys. **83**, 1057 (2011).
[3] C.-K. Chiu, J. C. Y. Teo, A. P. Schnyder, and S. Ryu, Classification of topological quantum matter with symmetries, Rev. Mod. Phys. **88**, 035005 (2016).
[4] A. Bansil, H. Lin, and T. Das, Colloquium: Topological band theory, Rev. Mod. Phys. **88**, 021004 (2016).
[5] L. Lu, J. D. Joannopoulos, and M. Soljačić, Topological photonics, Nat. Photonics **8**, 821 (2014).
[6] L. Lu, J. D. Joannopoulos, and M. Soljacic, Topological states in photonic systems, Nat. Phys. **12**, 626 (2016).
[7] S. D. Huber, Topological mechanics, Nat. Phys. **12**, 621 (2016).
[8] E. Prodan and C. Prodan, Topological Phonon Modes and Their Role in Dynamic Instability of Microtubules, Phys. Rev. Lett. **103**, 248101 (2009).
[9] C. L. Kane and T. C. Lubensky, Topological boundary modes in isostatic lattices, Nat. Phys. **10**, 39 (2014).
[10] B. G.-g. Chen, N. Upadhyaya, and V. Vitelli, Nonlinear conduction via solitons in a topological mechanical insulator, Proc. Natl. Acad. Sci. U.S.A. **111**, 13004 (2014).
[11] Z. Yang, F. Gao, X. Shi, X. Lin, Z. Gao, Y. Chong, and B. Zhang, Topological Acoustics, Phys. Rev. Lett. **114**, 114301 (2015).
[12] P. Wang, L. Lu, and K. Bertoldi, Topological Phononic Crystals with One-Way Elastic Edge Waves, Phys. Rev. Lett. **115**, 104302 (2015).
[13] M. Xiao, W.-J. Chen, W.-Y. He, and C. T. Chan, Synthetic gauge flux and Weyl points in acoustic systems, Nat. Phys. **11**, 920 (2015).
[14] L. M. Nash, D. Kleckner, A. Read, V. Vitelli, A. M. Turner, and W. T. M. Irvine, Topological mechanics of gyroscopic metamaterials, Proc. Natl. Acad. Sci. U.S.A. **112**, 14495 (2015).

[15] R. Süsstrunk and S. D. Huber, Observation of phononic helical edge states in a mechanical topological insulator, Science **349**, 47 (2015).

[16] S. H. Mousavi, A. B. Khanikaev, and Z. Wang, Topologically protected elastic waves in phononic metamaterials, Nat. Commun. **6**, 8682 (2015).

[17] R. Fleury, A. B. Khanikaev, and A. Alù, Floquet topological insulators for sound, Nat. Commun. **7**, 11744 (2016).

[18] D. Z. Rocklin, B. G.-g. Chen, M. Falk, V. Vitelli, and T. C. Lubensky, Mechanical Weyl Modes in Topological Maxwell Lattices, Phys. Rev. Lett. **116**, 135503 (2016).

[19] C. He, X. Ni, H. Ge, X.-C. Sun, Y.-B. Chen, M.-H. Lu, X.-P. Liu, and Y.-F. Chen, Acoustic topological insulator and robust one-way sound transport, Nat. Phys. **12**, 1124 (2016).

[20] J. Lu, C. Qiu, L. Ye, X. Fan, M. Ke, F. Zhang, and Z. Liu, Observation of topological valley transport of sound in sonic crystals, Nat. Phys. **13**, 369 (2016).

[21] R. Süsstrunk and S. D. Huber, Classification of topological phonons in linear mechanical metamaterials, Proc. Natl. Acad. Sci. U.S.A. **113**, E4767 (2016).

[22] P. Brüesch, *Phonons: Theory and Experiments II. Experiments and Interpretation of Experimental Results*, Springer Series in Solid-State Sciences vol. 65 (Springer, Berlin, 1986).

[23] O. Delaire, I. I. Al-Qasir, A. F. May, C. W. Li, B. C. Sales, J. L. Niedziela, J. Ma, M. Matsuda, D. L. Abernathy, and T Berlijn, Heavy-impurity resonance, hybridization, and phonon spectral functions in $Fe_{1-x}M_xSi(M = Ir, Os)$, Phys. Rev. B **91**, 094307 (2015).

[24] X. Zhu, Y. Cao, S. Zhang, X. Jia, Q. Guo, F. Yang, L. Zhu, J. Zhang, E. W. Plummer, and J. Guo, High resolution electron energy loss spectroscopy with two-dimensional energy and momentum mapping, Rev. Sci. Instrum. **86**, 083902 (2015).

[25] L. Zhang, J. Ren, J.-S. Wang, and B. Li, Topological Nature of the Phonon Hall Effect, Phys. Rev. Lett. **105**, 225901 (2010).

[26] N. Li, J. Ren, L. Wang, G. Zhang, P. Hänggi, and B. Li, Colloquium: Phononics: Manipulating heat flow with electronic analogs and beyond, Rev. Mod. Phys. **84**, 1045 (2012).

[27] Y. Liu, Y. Xu, S.-C. Zhang, and W. Duan, Model for topological phononics and phonon diode, Phys. Rev. B **96**, 064106 (2017).

[28] W.-C. Ji and J.-R. Shi, Topological phonon modes in a two-dimensional wigner crystal, Chin. Phys. Lett. **34**, 036301 (2017).

[29] S. Murakami, Phase transition between the quantum spin hall and insulator phases in 3d: Emergence of a topological gapless phase, New J. Phys. **9**, 356 (2007).

[30] X. Wan, A. M. Turner, A. Vishwanath, and S. Y. Savrasov, Topological semimetal and Fermi-arc surface states in the electronic structure of pyrochlore iridates, Phys. Rev. B **83**, 205101 (2011).

[31] S.-Y. Xu, I. Belopolski, N. Alidoust, M. Neupane, G. Bian, C. Zhang, R. Sankar, G. Chang, Z. Yuan, C.-C. Lee *et al.*, Discovery of a Weyl fermion semimetal and topological Fermi arcs, Science **349**, 613 (2015).

[32] B. Q. Lv, H. M. Weng, B. B. Fu, X. P. Wang, H. Miao, J. Ma, P. Richard, X. C. Huang, L. X. Zhao, G. F. Chen *et al.*, Experimental Discovery of Weyl Semimetal TaAs, Phys. Rev. X **5**, 031013 (2015).

[33] L. Lu, Z. Wang, D. Ye, L. Ran, L. Fu, J. D. Joannopoulos, and M. Soljačić, Experimental observation of weyl points, Science **349**, 622 (2015).

[34] A. A. Soluyanov, D. Gresch, Z. Wang, Q. Wu, M. Troyer, X. Dai, and B. A. Bernevig, Type-ii weyl semimetals, Nature (London) **527**, 495 (2015).

[35] A. A. Burkov, Topological semimetals, Nat. Mater. **15**, 1145 (2016).

[36] K. Deng, G. Wan, P. Deng, K. Zhang, S. Ding, E. Wang, M. Yan, H. Huang, H. Zhang, Z. Xu, J. Denlinger, A. Fedorov, H. Yang, W. Duan, H. Yao, Y. Wu, S. Fan, H. Zhang, X. Chen, and S. Zhou, Experimental observation of topological fermi arcs in type-ii Weyl semimetal $MoTe_2$, Nat. Phys. **12**, 1105 (2016).

[37] B. Bradlyn, J. Cano, Z. Wang, M. G. Vergniory, C. Felser, R. J. Cava, and B. A. Bernevig, Beyond dirac and Weyl fermions: Unconventional quasiparticles in conventional crystals, Science **353**, aaf5037 (2016).

[38] R. M. Geilhufe, S. S. Borysov, A. Bouhon, and A. V. Balatsky, Data mining for three-dimensional organic dirac materials: Focus on space group 19, Sci. Rep. **7**, 7298 (2017).

[39] Z. K. Liu, B. Zhou, Y. Zhang, Z. J. Wang, H. M. Weng, D. Prabhakaran, S.-K. Mo, Z. X. Shen, Z. Fang, X. Dai *et al.*, Discovery of a three-dimensional topological dirac semimetal, Na_3Bi, Science **343**, 864 (2014).

[40] G. Xu, H. Weng, Z. Wang, X. Dai, and Z. Fang, Chern Semimetal and the Quantized Anomalous Hall Effect in $HgCr_2Se_4$, Phys. Rev. Lett. **107**, 186806 (2011).

[41] C. Fang, M. J. Gilbert, X. Dai, and B. A. Bernevig, Multi-Weyl Topological Semimetals Stabilized by Point Group Symmetry, Phys. Rev. Lett. **108**, 266802 (2012).

[42] W.-J. Chen, M. Xiao, and C. T. Chan, Experimental observation of robust surface states on photonic crystals possessing single and double Weyl points, arXiv:1512.04681.

[43] S.-M. Huang, S.-Y. Xu, I. Belopolski, C.-C. Lee, G. Chang, T.-R. Chang, B. Wang, N. Alidoust, G. Bian, and M. Neupane *et al.*, New type of Weyl semimetal with quadratic double Weyl fermions, Proc. Natl. Acad. Sci. U.S.A. **113**, 1180 (2016).

[44] L. Pauling and A. M. Soldate, The nature of the bonds in the iron silicide, FeSi, and related crystals, Acta Crystallogr. **1**, 212 (1948).

[45] Y. N. Zhao, H. L. Han, Y. Yu, W. H. Xue, and T. Gao, First-principles studies of the electronic and dynamical properties of monosilicides MSI (M = Fe, Ru, Os), Europhys. Lett. **85**, 47005 (2009).

[46] X. Gonze and C. Lee, Dynamical matrices, born effective charges, dielectric permittivity tensors, and interatomic force constants from density-functional perturbation theory, Phys. Rev. B **55**, 10355 (1997).

[47] G. Kresse and J. Furthmüller, Efficient iterative schemes for *ab initio* total-energy calculations using a plane-wave basis set, Phys. Rev. B **54**, 11169 (1996).

[48] A. A. Soluyanov and D. Vanderbilt, Computing topological invariants without inversion symmetry, Phys. Rev. B **83**, 235401 (2011).
[49] R. Yu, X. L. Qi, A. Bernevig, Z. Fang, and X. Dai, Equivalent expression of $\mathbb{Z}_2$ topological invariant for band insulators using the non-Abelian Berry connection, Phys. Rev. B **84**, 075119 (2011).
[50] W. Gao, M. Lawrence, B. Yang, F. Liu, F. Fang, B. Béri, J. Li, and S. Zhang, Topological Photonic Phase in Chiral Hyperbolic Metamaterials, Phys. Rev. Lett. **114**, 037402 (2015).
[51] See Supplemental Material at http://link.aps.org/supplemental/10.1103/PhysRevLett.120.016401 for more detailed discussions.
[52] A. Togo and I. Tanaka, First principles phonon calculations in materials science, Scr. Mater. **108**, 1 (2015).
[53] M. P. L. Sancho, J. M. Lopez Sancho, J. M. L. Sancho, and J. Rubio, Highly convergent schemes for the calculation of bulk and surface Green functions, J. Phys. F **15**, 851 (1985).
[54] M. P. L. Sancho, J. M. Lopez Sancho, and J. Rubio, Quick iterative scheme for the calculation of transfer matrices: application to Mo (100), J. Phys. F **14**, 1205 (1984).
[55] Q. Wu, S. Zhang, H.-F. Song, M. Troyer, and A. A. Soluyanov, WannierTools: An open-source software package for novel topological materials, arXiv:1703.07789.
[56] C. Fang, L. Lu, J. Liu, and L. Fu, Topological semimetals with helicoid surface states, Nat. Phys. **12**, 936 (2016).
[57] R. Wolfe, J. H. Wernick, and S. E. Haszko, Thermoelectric properties of FeSi, Phys. Lett. **19**, 449 (1965).
[58] B. C. Sales, O. Delaire, M. A. McGuire, and A. F. May, Thermoelectric properties of Co-, Ir-, and Os-doped FeSi alloys: Evidence for strong electron-phonon coupling, Phys. Rev. B **83**, 125209 (2011).
[59] P. A. Frigeri, D. F. Agterberg, A. Koga, and M. Sigrist, Superconductivity without Inversion Symmetry: MnSi versus $CePt_3Si$, Phys. Rev. Lett. **92**, 097001 (2004).
[60] M. Mohr, J. Maultzsch, E. Dobardžić, S. Reich, I. Milošević, M. Damnjanović, A. Bosak, M. Krisch, and C. Thomsen, Phonon dispersion of graphite by inelastic x-ray scattering, Phys. Rev. B **76**, 035439 (2007).
[61] U. Harten and J. P. Toennies, Surface phonons on GaAs (110) measured by inelastic helium atom scattering, Europhys. Lett. **4**, 833 (1987).
[62] L. Wu, M. Salehi, N. Koirala, J. Moon, S. Oh, and N. P. Armitage, Quantized Faraday and Kerr rotation and axion electrodynamics of a 3D topological insulator, Science **354**, 1124 (2016).
[63] L. Wu, W.-K. Tse, M. Brahlek, C. M. Morris, R. V. Aguilar, N. Koirala, S. Oh, and N. P. Armitage, High-Resolution Faraday Rotation and Electron-Phonon Coupling in Surface States of the Bulk-Insulating Topological Insulator $Cu_{0.02}Bi_2Se_3$, Phys. Rev. Lett. **115**, 217602 (2015).
[64] A. Chaudhuri, A. Kundu, D. Roy, A. Dhar, J. L Lebowitz, and H. Spohn, Heat transport and phonon localization in mass-disordered harmonic crystals, Phys. Rev. B **81**, 064301 (2010).
[65] W. Kress, F. W. de Wette, W. Kress, and F. W. de Wette, *Surface Phonons*, Springer Series in Surface Sciences 21, 1st ed. (Springer-Verlag, Heidelberg, Berlin1991).
[66] G. Resta, S.-T. Pi, X. Wan, and S. Y. Savrasov, High surface conductivity of Fermi arc electrons in Weyl semimetals, arXiv:1708.02415.
[67] S. Zhang, J. Guan, X. Jia, B. Liu, W. Wang, F. Li, L. Wang, X. Ma, Q. Xue, J. Zhang *et al.*, Role of $SrTiO_3$ phonon penetrating into thin FeSe films in the enhancement of superconductivity, Phys. Rev. B **94**, 081116 (2016).
[68] G. Chang, S.-Y. Xu, B. J. Wieder, D. S. Sanchez, S.-M. Huang, I. Belopolski, T.-R. Chang, S. Zhang, A. Bansil, H. Lin, and M. Z. Hasan, Unconventional Chiral Fermions and Large Topological Fermi Arcs in RhSi, Phys. Rev. Lett. **119**, 206401 (2017).
[69] P. Tang, Q. Zhou, and S.-C. Zhang, Multiple Types of Topological Fermions in Transition Metal Silicides, Phys. Rev. Lett. **119**, 206402 (2017).

Double-Weyl phonons in transition-metal monosilicides: Supplemental material

Tiantian Zhang,[1] Zhida Song,[1] A.Alexandradinata,[2] Hongming Weng,[1,3] Chen Fang,[1,*] Ling Lu,[1,†] and Zhong Fang[1,3]

[1]*Institute of Physics, Chinese Academy of Sciences/Beijing National Laboratory for Condensed Matter Physics, Beijing 100190, China*

[2]*Department of Physics, Yale University, New Haven, Connecticut 06520, USA*

[3]*Collaborative Innovation Center of Quantum Matter, Beijing, 100084, China*

[*] cfang@iphy.ac.cn

[†] linglu@iphy.ac.cn

CONTENTS

I. PHONON SPECTRA OF THE MSI FAMILY WITH LO-TO SPLITTING

MSi family materials have similar band dispersions at the high symmetry points due to the same space group $P2_13$. The irreducible representation for the optical bands of MSi family at Γ point is : $\Gamma = 2A + 2E + 5T$. A, E and T represent single, double and triple degeneracies respectively. The phonon band structures for MSi family are showed in Fig.1.(a-d), and apparently, the MSi family materials all have three-fold crossing at Γ points (spin-1 Weyl) and four-degenerated crossing bands (charge-2 Dirac) at R point.

It is well known that longitudinal optical (LO) phonons and transverse optical (TO) phonons split in the vicinity of Γ point for ionic crystals, since the Coulomb interaction between the charged ions will raise the frequency of LO branch. Such LO-TO splitting is in fact due to the coupling between photons and TO phonons, forming phonon polaritons. However, exactly at the Γ point, the 3-fold degeneracy is strictly guaranteed by the space group. As a result, the LO-TO splitting will not influence the topological properties of MSi. The phonon band structures for MSi family are showed in Fig. 1.(a-e). The red solid lines are phonon spectra without considering ions being charged, the black dashed lines are phonon spectra considering ions being charged.

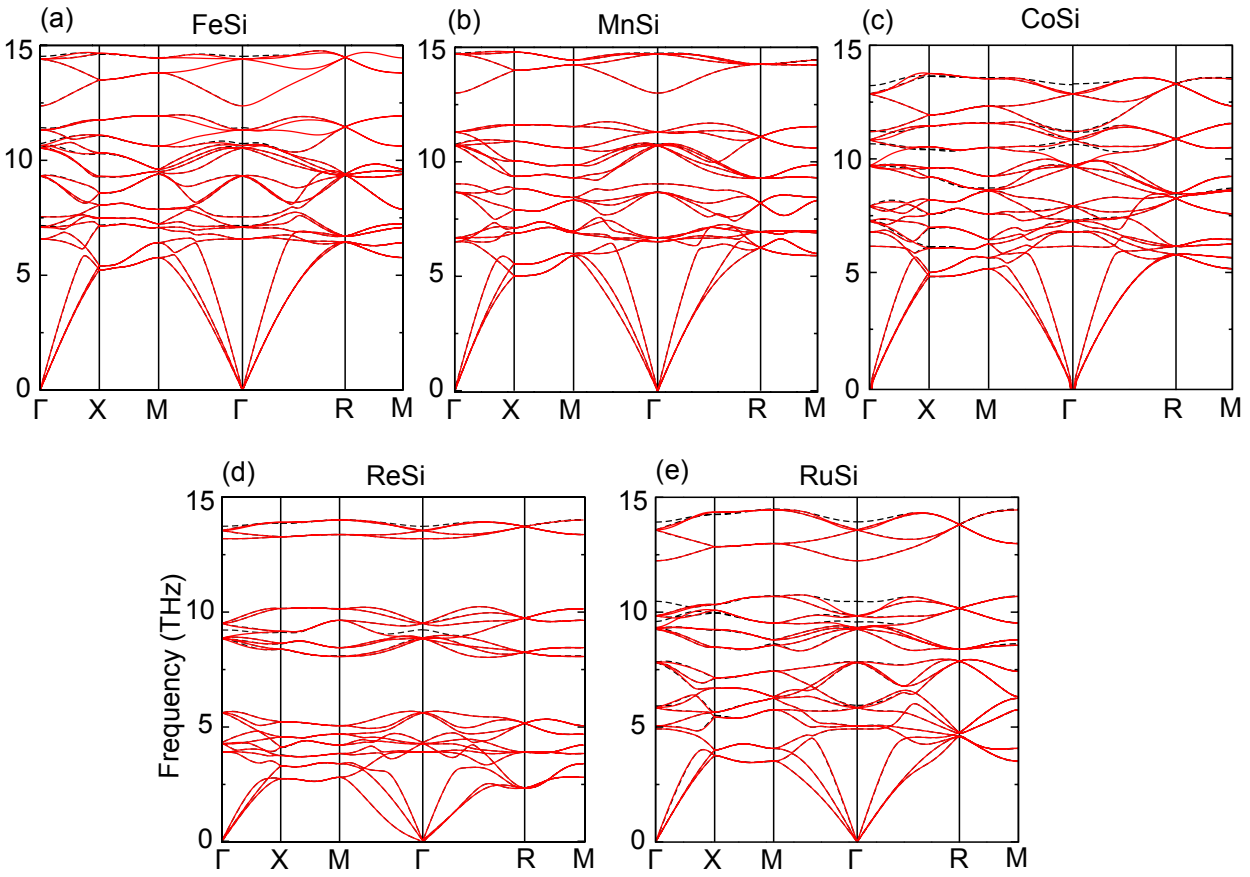

Figure 1. MSi family phonon dispersions with and without LO-TO splitting. (a-d) show the phonon dispersions of FeSi, MnSi, CoSi, ReSi and RuSi. The red solid lines are phonon spectra without considering LO-TO splitting, as in the main text. The black dashed lines are phonon spectra considering LO-TO splitting.

II. CHERN-NUMBER CALCULATIONS BY WILSON-LOOP METHOD

Chern numbers are defined in a closed two-dimensional band surface The Chern numbers in this paper were calculated the by following this approach. First of all, we discretized the sphere into 1D loops and they are parametrized by azimuth angle φ and elevation angle θ. Then, we calculated the Berry phase by using the wave functions around the gapless point, and the trace of the Berry phase corresponds to the Wannier centers $\langle\varphi\rangle$. In Fig.2, φ is the azimuth angle varying from 0 to 2π and θ is the elevation angle varying from 0 to π for the spherical coordinate. When θ varies for a cycle, the Wannier center $\langle\varphi\rangle$ can only shift an integer multiple of 2π and the multiple number is equal to the summed Chern numbers of

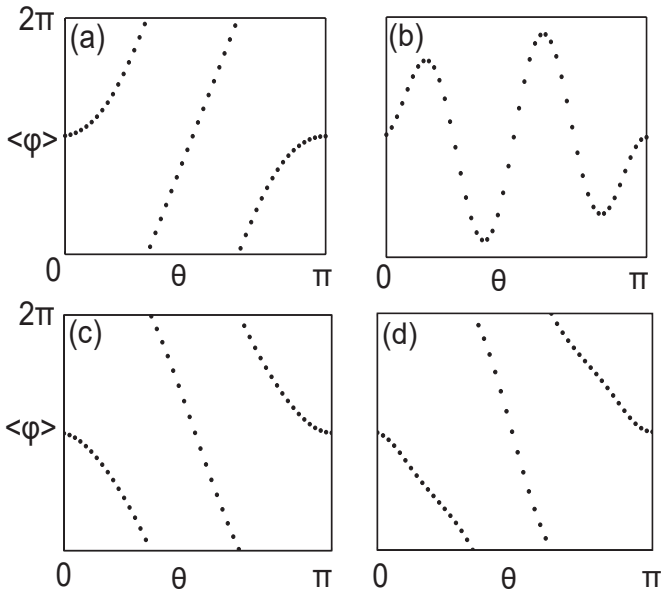

Figure 2. Motion of the Wannier center around the spheres enclosing double-Weyl points. φ is the azimuth angle varying from 0 to 2π and θ is the elevation angle varying from 0 to π. Panel (a)-(c): Wilson loop for the 22nd, 23rd, 24th band at Γ point (spin-1 Weyl). (d): Wilson loop for summing over the 22nd and 23rd band phases at R point (double-Weyl).

the calculated bands. Since the Wannier centers shift by 4π, 0, -4π in Fig.2.(a)-(c), we can figure out that the Chern numbers for the 22nd-24th band are +2,0,-2 and there is a spin-1 Weyl node at Γ point. The shift of -4π in Fig.2.(d) are calculated by summing over the 21st and 22nd band, and the result shows that there is a charge-2 Dirac point at R momentum.

III. PHONON SURFACE STATES FOR MSI FAMILY

Fig. 3 shows the phonon surface states and arcs for the MSi family on the (001) surface. We can see that MSi family materials have similar surface states due to their identical topological invariant at Γ and R momenta. The two surface arcs rotate around those two double-Weyl points as frequency decreases from f1 to f3, which demonstrates the existence of double-helical surface states.

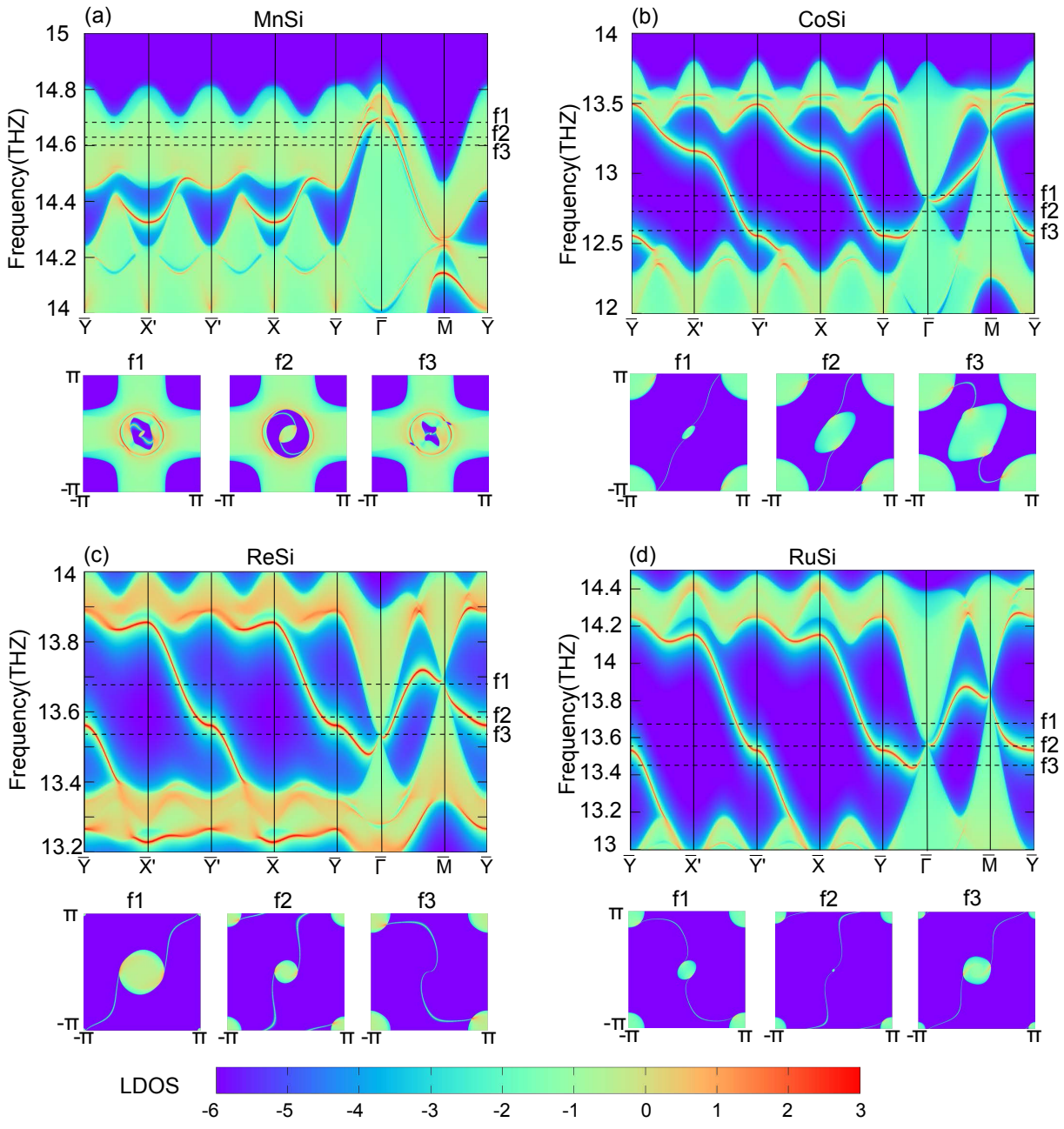

Figure 3. Phonon surface states and arcs for the rest of MSi family. (a-d) show the surface states of MnSi, CoSi, ReSi and RuSi. The semi-infinite slab for MnSi is along (00-1) direction, the other materials are along (001) direction. All the arcs rotate around Γ point as the frequency decreases.

IV. DETAILS FOR $k \cdot p$ MODEL

The generic form of the effective Hamiltonian at Γ and R points can be written down up to the 1st order of k. As we discussed in the text, the important symmetries (generators) of the little group at Γ point are time-reversal symmetry τ, three-fold rotation symmetry C_3 along (111) direction and screw rotation symmetry $\{C_{2y}|(0, \frac{1}{2}, \frac{1}{2})\}$ along the x axis. In a set of real basis, the representation of those symmetries can be written as the corresponding space group operation like:

$\tau = \kappa \otimes I_{3\times 3}$, where κ is the complex conjugation operator,

$$C_3 = \begin{pmatrix} 0 & 0 & 1 \\ 1 & 0 & 0 \\ 0 & 1 & 0 \end{pmatrix},$$

$$C_{2y} = \begin{pmatrix} -1 & 0 & 0 \\ 0 & 1 & 0 \\ 0 & 0 & -1 \end{pmatrix}.$$

The generic form of the effective Hamiltonian at Γ point is as following:

$$H(k) = A \cdot \begin{pmatrix} 0 & ik_z & -ik_y \\ -ik_z & 0 & ik_x \\ ik_y & -ik_x & 0 \end{pmatrix} = A \cdot \mathbf{k} \cdot \mathbf{L} \text{ , } A \text{ is a real constant.}$$

The generating elements of the little group at R point are time-reversal symmetry τ, three-fold rotation symmetry C_3 along (111) direction, and screw rotation symmetry $\{C_{2x}|(\frac{1}{2}, \frac{1}{2}, 0)\}$ along the x axis. The representation of those symmetries are : $\tau = \kappa\sigma_0 \otimes \sigma_x$, and there are two different kinds of representaions for C_3. The representations for the generators are :

$$C_{31} = sin(\tfrac{\pi}{4}) \begin{pmatrix} cos(\frac{\pi}{12}) & cos(\frac{\pi}{12}) & sin(\frac{\pi}{12}) & sin(\frac{\pi}{12}) \\ sin(\frac{\pi}{12}) & -sin(\frac{\pi}{12}) & -cos(\frac{\pi}{12}) & cos(\frac{\pi}{12}) \\ -sin(\frac{\pi}{12}) & -sin(\frac{\pi}{12}) & cos(\frac{\pi}{12}) & cos(\frac{\pi}{12}) \\ cos(\frac{\pi}{12}) & -cos(\frac{\pi}{12}) & sin(\frac{\pi}{12}) & -sin(\frac{\pi}{12}) \end{pmatrix},$$

$$C_{32} = \tfrac{1}{2} \begin{pmatrix} -1 & -1 & 1 & 1 \\ 1 & -1 & 1 & -1 \\ -1 & -1 & -1 & -1 \\ -1 & 1 & 1 & -1 \end{pmatrix}$$

$$C_{2x} = \begin{pmatrix} 0 & 0 & 1 & 0 \\ 0 & 0 & 0 & -1 \\ -1 & 0 & 0 & 0 \\ 0 & 1 & 0 & 0 \end{pmatrix}$$

Since two of the representations can get the same form of effective Hamiltonian, we only take C_{31} as an example. After a unitary transformation, we can get a block form of C_{31} and C_{2x}:

$$C_{31} = sin(\tfrac{\pi}{4}) \begin{pmatrix} e^{-i\frac{\pi}{12}} & e^{-i\frac{\pi}{12}} & 0 & 0 \\ ie^{-i\frac{\pi}{12}} & -ie^{-i\frac{\pi}{12}} & 0 & 0 \\ 0 & 0 & e^{i\frac{\pi}{12}} & e^{i\frac{\pi}{12}} \\ 0 & 0 & -ie^{i\frac{\pi}{12}} & ie^{i\frac{\pi}{12}} \end{pmatrix},$$

$$C_{2x} = -i\sigma_z \otimes \sigma_3$$

So the generic form of the effective Hamiltonian at R point is:

$$H(k) = B \begin{pmatrix} -k_x & k_z + ik_y & 0 & 0 \\ k_z - ik_y & k_x & 0 & 0 \\ 0 & 0 & k_x & -k_z + ik_y \\ 0 & 0 & -k_z - ik_y & -k_x \end{pmatrix}$$

After a unitary transformation, $H(k) = B \begin{pmatrix} \mathbf{k}\cdot\sigma & 0 \\ 0 & \mathbf{k}\cdot\sigma \end{pmatrix}$, B is a real constant.

Such an effective model can be used for further low-energy properties study of MSi family. After space-group symmetry analysis, we find that space group no. 205, no. 212 and no. 213 (supergroups of no. 198) all share the same $k \cdot p$ models (at Γ and R points) as those derived above. So crystals with those space-group symmetries will have similar topological properties and surface states.

V. ELECTRONIC BAND STRUCTURE

Fig. 4 shows the electronic band structure of FeSi.

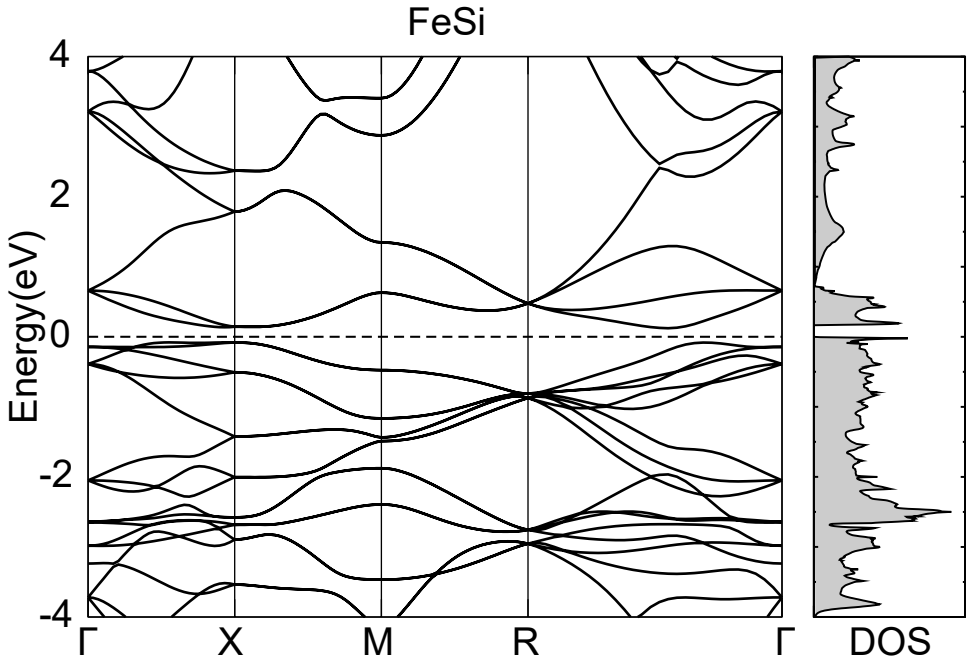

Figure 4. FeSi electronic band structure

VI. ATOMIC VIBRATIONAL MODES (ANIMATIONS)

As we just mentioned in the text, phonons are quantized excited vibrational states of interacting atoms. It is curious to see how the atoms vibrate in the topological modes, so we make animations in the vicinity of Γ and R point (see the details in the attachment). We choose three acoustic branches and highest three optical bands who's Chern numbers are $0, \pm 2$ at $\mathbf{k}_1 = (0, 0, 0.01)$ point. At $\mathbf{k}_1$ point, the propagation direction is along z axis. So the longitudinal acoustic wave who's $C = 0$ has vibrations along z axis, and the $C = \pm 2$ transverse acoustic wave has vibrations rotates aroud z axis with right/left-handed chirality. The highest four optical branches who's chern numbers are $+1, +1, -1, -1$ at $\mathbf{k}_2 = (0.49, 0.49, 0.49)$. Although the optical phonons have out-of-phase movements and it is hard to follow the trajectory, we still can figure out that two vibration modes with opposite Chern numbers have opposite chirality rotations for each atom.

VII. ANHARMONIC EFFECTS

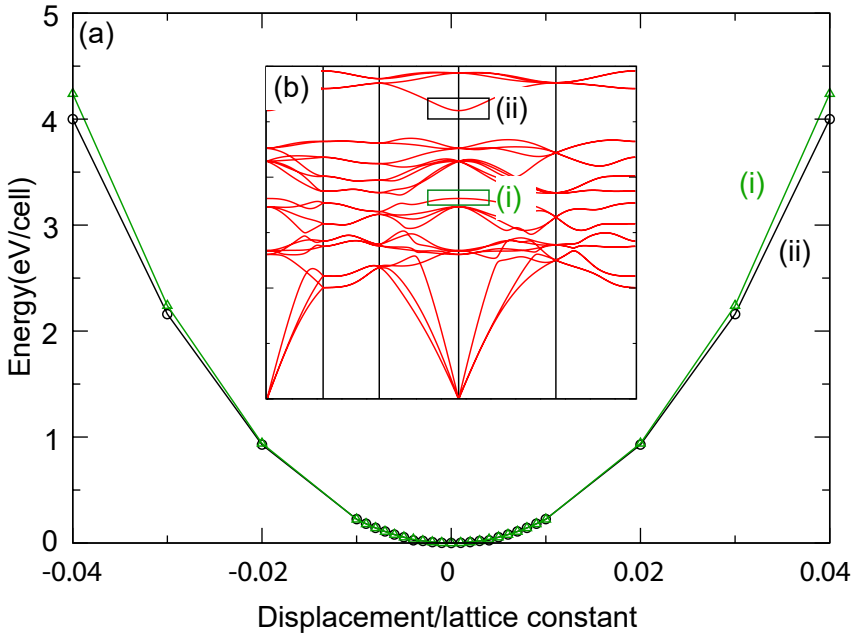

Figure 5. (a) is an analysis of phonon anharmonicity in MnSi using an energy-displacement curve. The green line is the mode with four Mn atoms vibrate along (-1,-1,-1), (1,1,-1), (1,-1,1), (-1,1,1) directions respectively, and the corresponding mode (i) is showed in the figure (b). The black line is the mode with four Si atoms vibrate along (1,1,1), (-1,-1,1), (-1,1,-1), (1,-1,-1) directions respectively, and the corresponding mode (ii) is also showed in the figure (b).

Anharmonic effects usually manifests at high temperatures and diminishes at low temperatures. In phonon scattering experiments, the samples are usually kept at a low temperature (4.2K for liquid helium cooling system). The anharmonic effects should be weak at such a low temperature.

In order to theoretically investigate the phonon anhamonicity effects, we calculated the distortion energy versus atom displacements for MnSi. The green line shows the distortion energy versus displacement of Mn atom in MnSi, and the corresponding vibration mode is labeled by a green box in Fig. 5. (b). The black line shows the distortion energy versus displacement of Si atom, and the corresponding vibration mode (ii) is labeled by a black box in Fig. 5. (b). Both the green line and black line are of parabolic shapes, indicating the validation of harmonicity at low temperature.

VIII. PHONON SPECTRUM IN MAGNETIC GROUND STATE

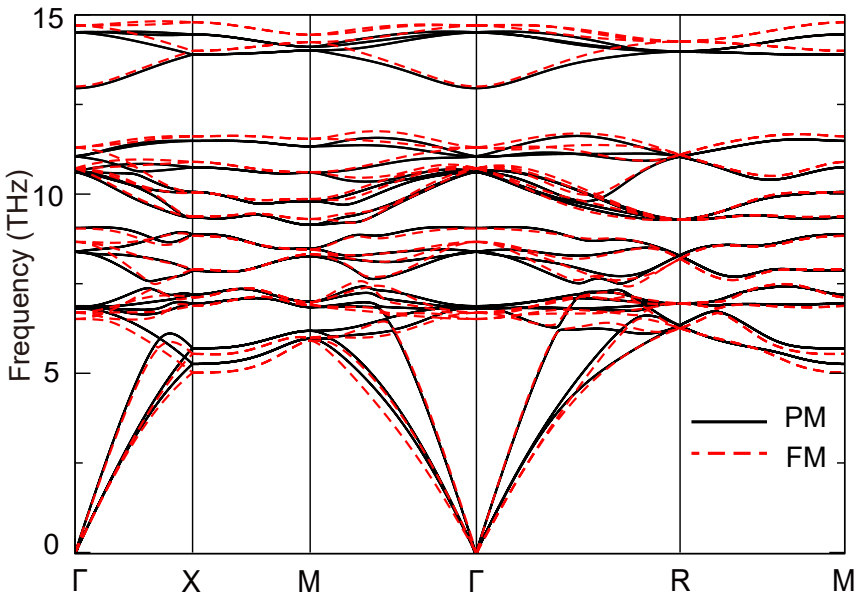

Figure 6. Phonon spectra for MnSi in both ferromagnetic phase and nonmagnetic phase. The black solid line is in a paramagnetic phase, and the red dashed line is in a ferromagnetic phase.

All the data above for MSi family materials are calculated in a paramagnetic(PM) phase. But MnSi will have an anti-ferromagnetic(AFM) phase below the Neel temperature of 60K, and change to a ferromagnetic(FM) phase when the temperature goes below 30K. There is no structure change in the magnetic phases; the space group is still No.198.

Magnetic structure breaks $\mathcal{T}$ of the crystal, especially for electrons. But the $\mathcal{T}$-breaking for phonons is very weak if not negligible, because phonons are neutral particles and do not couple to magnetic field to the first order.

In our theoretical frame work, the electronic magnetic ordering only modifies the amplitudes of the force constants between atoms. But the force constants are still real numbers, meaning no $\mathcal{T}$-breaking for phonons. We calculated the phonon spectra of MnSi in the FM phase(red dashed lines in Fig. 6) and PM phase(black solid lines in Fig.6). There is only frequency shifts.

If we assume $\mathcal{T}$ is broken for phonons, the Spin-1 Weyl at Gamma point (only protected by space group symmetry) will still exist, but the Charge-2 Dirac point at R will split into two Spin-1/2 Weyl points.